Soil Dynamics and Earthquake Engineering 126 (2019) 105784

Contents lists available at ScienceDirect

Soil Dynamics and Earthquake Engineering

journal homepage: www.elsevier.com/locate/soildyn

Near-field velocity pulse-like ground motions on February 6, 2018 M_W6.4 Hualien, Taiwan earthquake and structural damage implications

Kun Ji[a], Yefei Ren[a,*], Ruizhi Wen[a], Chun-Hsiang Kuo[b]

[a] Key Laboratory of Earthquake Engineering and Engineering Vibration, Institute of Engineering Mechanics, China Earthquake Administration, No. 29 Xuefu Road, Harbin, Heilongjiang, 150080, People's Republic of China

[b] National Center for Research on Earthquake Engineering, No. 200, Section 3, Xinhai Road, Taipei, 10668, Taiwan

ARTICLE INFO

Keywords:
Hualien earthquake
Velocity pulse-like records
Pulse period
Ductility demand

ABSTRACT

The February 6, 2018 Hualien Taiwan Earthquake (M_w6.4) had caused serious fatalities and severe building damages in Hualien city. Substantial near-field velocity pulse-like ground motions were probably one of the important factors. We used the continuous wavelet transforms method to identify the velocity pulse-like ground motions from orthogonal components of all the recorded ground motions. The identification results were in agreement with the contour map of pulse-like occurrence probability according to two prediction models for non-strike-slip faults. After verification using method based on the energy content of significant velocities pulses, 16 near-field recordings were recognized as the pulse-like ones, and the pulse period (T_p) was then determined individually. It was found that the extracted values of T_p were generally longer than the prediction value given by the empirical regression model based on the NGA-West2 dataset. The single and multiple degrees of freedom (SDOF and MDOF, respectively) systems were implemented in the computation of inelastic demand and story ductility demand. The results indicated the followings: (1) For the identified pulse-like records, the inelastic demand of SDOF with oscillator period T less than $0.6T_p$ is much more significant than that for non-pulse-like records when the SDOF nonlinearity level increases. The mean inelastic displacement ratio curve is approximately one standard deviation higher than the mean prediction value in the $0.1 < T/T_P < 0.5$ range. (2) The maximum ductility demand exists at the bottom story of the 7-story,9-story and 11-story MDOF structure subject to the pulse-like records. For the case of reduced shear strength and stiffness at the bottom story due to removed infill walls, the bottom ductility demand reach more than 10.0 under pulse-like records. These findings support the supposition that large ductility demand and the bottom soft-story mechanism under near-field velocity pulse-like ground motions were the main reasons for severe structural damage of the four near-field mid-rise RC buildings during the Hualien earthquake.

1. Introduction

A moderate M_w6.4 earthquake struck the Taiwan Hualien City on February 6, 2018. It occurred offshore (24.1007°N, 121.7296°E) at a focal depth of 6.31 km and resulted in surface rupture close to the downtown area of Hualien City. Despite the moderate magnitude, it caused 17 deaths and 298 injuries. Moreover, concern was raised regarding four mid-rise reinforced concrete (RC) buildings that were partially collapsed or tilted during this event causing a number of fatalities.

For ground motions in the near-fault zone, possible velocity pulse-like records were the consequences of the directivity effects and/or the permanent ground displacement at the site resulting from tectonic movement which is termed 'fling-step' [1]. The Hualien earthquake occurred in a complex tectonic area with a high background seismicity rate, where a complex fault-to-fault jumping rupture process was found according to the joint source inversion results [2]. It is indicated that the initial rupture started from a north-south (N–S) striking fault dipping to the west and propagated to the south with a high rupture speed. The rupture then jumped to the shallower east-dipping Milun fault across the Hualien city, where severe surface cracks and most of the damaged buildings including the four collapsed ones were found. There is a high possibility that pulse-like records would be observed in the near-field area of Hualien earthquake.

Ground motions with strong velocity pulses are of special concern for structural engineers [3]. The substantial impact of near-field velocity pulse-like ground motions have been observed previously on a number of occasions: e.g., the Kobe (1995; Japan), Northridge (1994;

* Corresponding author.
E-mail addresses: jikun@iem.ac.cn (K. Ji), renyefei@iem.net.cn (Y. Ren), ruizhi@iem.ac.cn (R. Wen), chkuo@ncree.narl.org.tw (C.-H. Kuo).

https://doi.org/10.1016/j.soildyn.2019.105784
Received 9 November 2018; Received in revised form 27 June 2019; Accepted 29 July 2019

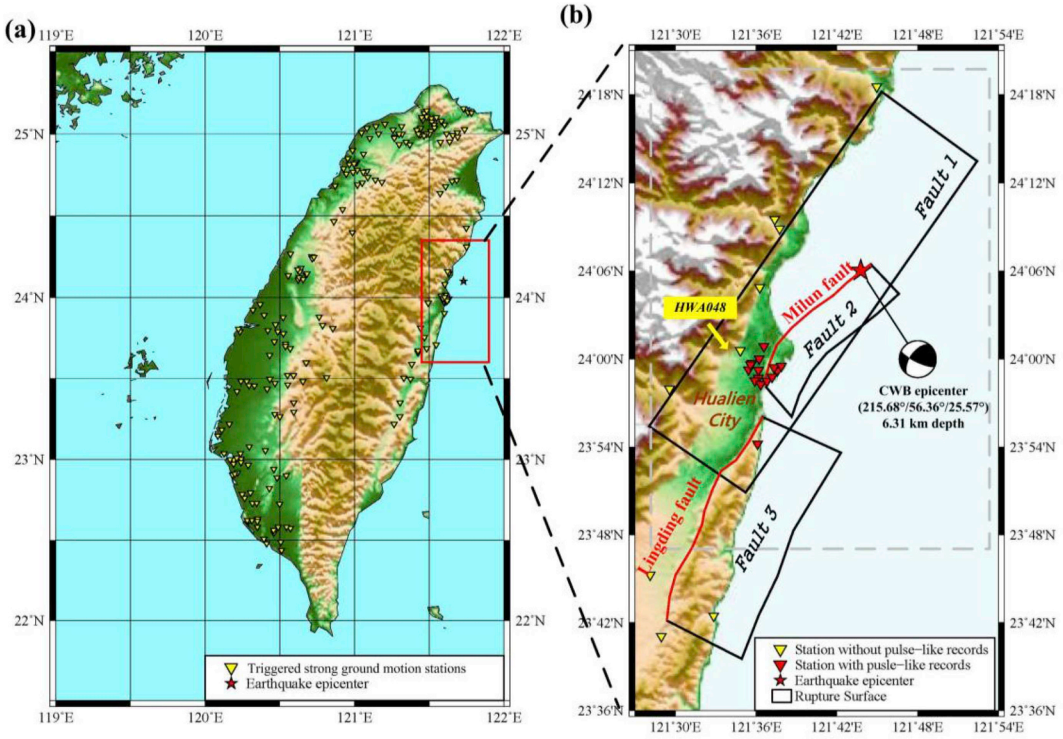

Fig. 1. (a) Strong ground motion stations triggered in M_w6.4 2018 Hualien earthquake. (b) Stations with/without identified pulse-like records in the near-field area (gray dashed rectangle); The epicenter provided by Central Weather Bureau(CWB) is represented with a red star. The three fault planes considered in this study are projected to the surface and labeled as Fault 1, 2 and 3 respectively. (For interpretation of the references to colour in this figure legend, the reader is referred to the Web version of this article.)

USA), Wenchuan (2008; China) and Chi-Chi (1999; Taiwan) earthquakes. During the 2016 Taiwan Meinong earthquake, one high-rise building was collapsed and caused more than 100 deaths that were attributed to velocity pulse-like ground motions [4]. Similar near-field pulse-like velocity records might be responsible for the serious structural damage during the Hualien earthquake [5].

Several studies have investigated the effects of near-fault pulse like ground motions on the inelastic displacement ratio (i.e., ratio of maximum inelastic displacement with respect to maximum elastic displacement demand using SDOF systems) [6–8]. The results indicated that the near-fault pulse-like ground motions may induce greater inelastic displacement demand, and could be classified as “aggressive” ones when the normalized vibration period T with respect to velocity pulse period T_p (T/T_p) is less than one [9]. A significant large inelastic demand for T/T_P ranges from 0.3 to 0.5 was observed concerning the wavelet algorithm method identified pulse-like records in the NGA-West1 database [8,10]. Furthermore, a prediction model was regressed for near-source pulse-like inelastic displacement ratio as a function of T/T_p according to fault-normal pulse-like records in NGA dataset [8]. Comparing the results between non-degrading and stiffness/strength degrading SDOF systems, the increments in the level of cyclic degradation increases the inelastic demands for systems with T shorter than T_p [7,11]. Wen et al. [12] investigated the inelastic displacement ratios with constant modified Park-Ang damage index proposed in Zhai et al [13]. Similar to previous studies, the near-fault pulse-like ground motions significantly increase the inelastic demand of structures with medium fundamental period. All the four collapsed buildings in Hualien earthquake are mid-rise (i.e., 7,10,11,12 stories) RC structure and probably be more vulnerable to the pulse-like ground motions according to the previous studies, which will be further verified in our study.

Behavior of moment-resisting frame structures subjected to the pulse-like near-fault ground motions were studied by MDOF systems [14,15]. Similar to the observation results in SDOF systems, the results indicated that the pulse-like records with $T/T_p < 1$ would produce increased inelastic displacement demands compared to the $T/T_p > 1$ case. A detailed assessment of seismic collapse risk shows that the predicted probability of collapse in 50 years for mid-rise modern RC buildings at a representative near-fault site is approximately 6%, which is significantly higher than the targeted 1% probability in current seismic design maps of the U.S [16]. For $T/T_p > 1$ case, the higher modes have a significant contribution, while for longer pulses ($T/T_p < 1$) their effect is small [14]. Records with fling effects were found to excite systems primarily in their fundamental mode while waveforms with forward directivity in the absence of fling caused higher modes to be activated [17]. In addition, ground motions with T_p longer than T of structure tend to be more destructive at lower bottom stories [16,17]. The four mid-rise buildings in Hualien Earthquake are all collapsed due to the similar crush or serious damage at bottom stories. In this paper, we tried to look into the pulse-like records in Hualien earthquake and the corresponding implications on the structural damage from this perspective.

First, the near-field records from the mainshock of the Hualien earthquake were analyzed to identify possible pulse-like ones using the wavelet transforms method. Two prediction models for non-strike-slip ruptures were utilized for computation of pulse-like occurrence probability contour map of the studied area and compared with identification results. The values of T_p and corresponding orientations in which the pulses were strongest were then computed and verified. To further illustrate the potential impact regarding the partially collapsed RC midrise buildings, SDOF and MDOF systems were implemented in the computation of the inelastic demand and story ductility demand concerning the near-field records of the Hualien earthquake.

2. Strong ground motion data

The epicenter of February 6, 2018 M_w 6.4 Hualien earthquake, was

located in the offshore area about 16.5 km north from Hualien City. The Central Weather Bureau (CWB) calculated the focal mechanism using the centroid moment tensor solution and broadband seismic data obtained in Taiwan. The strike/dip/rake were 215.68°/56.36°/25.57°. Joint inversion results show that the source of the Hualien earthquake was complex and contains three asperities on different fault systems [2]. As shown in Fig. 1, The slip started from an N–S striking west dipping fault (Fault 1) with a high rupture speed of approximately 3.0 km/s, then the rupture jumped to the Milun and Lingding faults (Fault 2 and Fault 3) with slow rupture speed of approximately 2.0 km/s. In other words, although most of the damaged buildings were found along the Milun fault, the movement on the Milun fault was passive and just part of a secondary branch of the major rupture system. These imply that the rupture on Fault 1, which started from the offshore area and propagated all the way toward the land (city of Hualien), is the main contributing factor for the possible pulse-like records. Nevertheless, the Milun fault and Linding fault also have an impact on the characteristic of the near-fault pulse-like records.

The raw strong ground motion data of the mainshock were provided by the Taiwan Central Weather Bureau (ftp://gdms.cwb.gov.tw/, last accessed on Oct 2018). Overall, 196 strong ground motion stations were triggered over Taiwan, as shown in Fig. 1(a). In this study, 21 stations within 30 km of epicenter distance were considered, as shown in the gray dashed rectangle region of Fig. 1(b). The boundary value was set as 30 km synthetically considering the amplitude of the records, the spatial distribution of the stations and the locations of three faults. Because severe surface breaks and cracks were observed along the Milun fault, it is necessary to recover the ground displacements in strong-motion recordings. The acceleration time histories were processed using the automatic baseline correction method proposed by Wu and Wu [18]. This method has been successfully applied in the process of the strong-motion data in the 1999 Chi-Chi, 2003 Chengkung, and 2006 Taitung earthquakes in the near-field region and the corresponding coseismic displacements were consistent with GPS measurements. The Butterworth band-pass filter was not applied in this study to avoid possible impact on the presence and shape of the identified velocity pulse and displacement recovery [19]. To evaluate the recovered displacements from strong motion stations, the results were compared with coseismic displacements measured with two continuous GPS stations in the studied area [20]. As shown in Table .1, the recovered displacements are close to the GPS measurements results considering the EW and NS component. The recovered displacement time histories were presented in Fig. 2.

3. Characteristics of pulse-like ground motions

3.1. Preliminary pulse-like ground motion recognition

The method based on wavelet transform algorithm was used in this paper for the identification of pulse-like ground motions. An earlier method using this algorithm proposed by Baker [21] in 2007 was usually used to identify the pulse-like ground motions in a single orientation (typically the fault-normal orientation). However, the pulse-like ground motions might be observed in orientations other than fault-normal especially for the non strike-slip ruptures of which the directivity is not obvious as strike-slip rupture. For Hualien earthquake, three non strike-slip faults were involved and the rupture mechanism is relatively complex. Therefore we utilized a wavelet algorithm based method proposed by Shahi and Baker [22] (hereafter called SB14 method) to preliminarily identify pulses at arbitrary orientations in multicomponent ground motions. After identifying the orientation at which the wavelet coefficients is maximum (hereafter called maximum pulse-like orientation), a new method proposed by Zhai et al(2018) [13] was then applied to validate the identification results which was based on the energy content of significant velocity pulses.

Table 1
Comparison of continuous Global Positioning System (GPS) Measurements and recovered displacements.

Station	Log(°)	Lat(°)	EW	NS
HWAL(GPS)	121.6135	23.9754	16.70 cm	43.20 cm
HWA019	121.6135	23.9750	15.77 cm	42.80 cm
PEPU(GPS)	121.6103	24.0179	−5.39 cm	−28.61 cm
HWA028	121.6096	24.0143	−10.42 cm	−30.16 cm

According to SB14 method, the continuous wavelet transforms were used for two orthogonal components of the ground motion to identify the orientations most likely to contain a pulse in the first step. The wavelet with the largest wavelet transform coefficients coefficient defined in Ref. [21] was selected as a potential pulse. Then, the wavelet with the largest coefficient nonadjacent to the selected coefficient was selected as the second potential pulse. This process was repeated to select five nonadjacent potential pulses. For each potential pulse, the velocity time history was rotated into the orientation in which the pulse was found. The maximum pulse-like orientation attributed to the orientation in which the maximum wavelet coefficient is found. Therefore for each studied recording, we would get five possible maximum pulse-like orientations. For each orientation, the selected wavelet was then subtracted from the original ground motion to yield a residual ground motion. The continuous wavelet transform of the residual ground motion is used to find the wavelet with highest coefficient that has the same scale as the original wavelet. This wavelet was then added to the original wavelet to refine the shape of the selected pulse. This step was repeated 10 times and used a combination of the 10 wavelets to define the shape of the extracted pulse. Then the extracted pulses were judged by the pulse indicator *PI* to determine whether they are strong enough to be classified as pulse-like. The peak ground motion velocity (*PGV*) and *PC* were used to define the *PI*, as indicated in Eq. (1) from Ref. [22].

$$PI = 9.384(0.76 - PC - 0.0616PGV)(PC + 6.914 \times 10^{-4}PGV - 1.072) - 6.179 \quad (1)$$

$$PC = 0.63 \times PGV\ ratio + 0.777 \times energy\ \text{ratio} \quad (2)$$

here, *PC* is the linear combination of two variables: the energy ratio and the *PGV* ratio between residual and original ground motions (Eq. (2)). Energy could be indicated by the cumulative squared velocity of the signal. In most cases, if the extracted pulse is significant, the residual *PGV* and energy is much lower after removing the pulses, and the corresponding *PGV* ratio and energy ratio would also be much lower. The smaller the *PC* value is, the more obvious the characteristic of the velocity pulse is. The ground motion is classified as pulse-like one when the indicator *PI* is positive. If we let $PI = 0$, we could plot the corresponding classification boundary as function of *PGV* and *PI* as shown in Fig. 3. The value of 20 cm/s is the suggested minimum *PGV* boundary by Ref. [22] to ensure the identified velocity pulses have engineering significance. A clear curved bounding domain could be found in the classification boundary of Fig. 3. It is worth noting the PGV threshold (20 cm/s) is learned from the NGA-west2 data rather than set arbitrarily like in Ref. [21].

Of the analyzed 21 stations in Fig.1(b), 15 were preliminarily classified as having pulse-like records (shown in bold in Table 2). The identified pulse period T_p, which is of special interest to engineer as discussed in the following part, exceeds 2.0s for all 14 stations except the HWA060 which were located far from other stations and Milun fault. The maximum pulse-like orientation is presented using azimuth. The velocity time-histories of the records rotated in the maximum pulse-like orientation were plotted in Fig. 4. Typical near-fault pulse-like strong ground motions were recorded at stations on both sides of the Milun fault. The maximum pulses were mostly in the fault-normal direction, especially near the southern portion of the Milun fault. Double-sided velocity pulses with large amplitude can be clearly

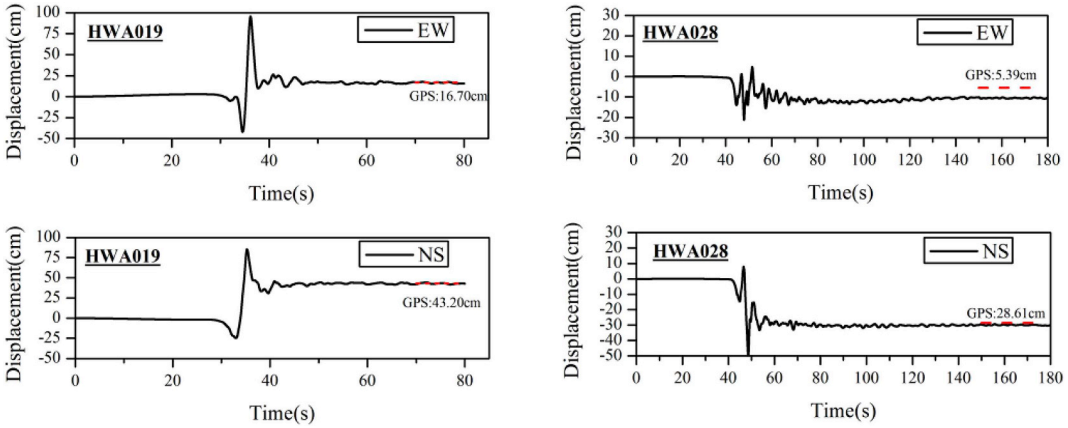

Fig. 2. The recovered displacement time histories in the east–west(EW) and north-west(NS) direction regarding HWA019 and HWA028 stations.

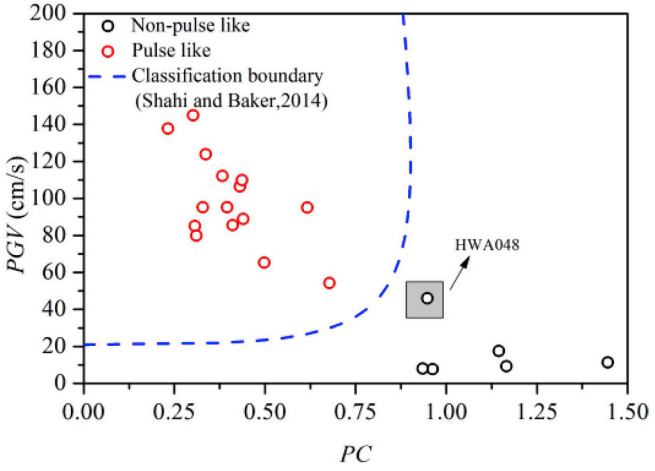

Fig. 3. *PGV* versus *PC* values for ground motions rotated in the maximum pulse-like orientation. The dashed line indicates the classification boundary in SB14 method [22].

observed and the PGV is reasonably high, i.e., > 40 cm/s, which is higher than the suggested classification boundary of 20 cm/s. The corresponding *PGV* and *PC* values of all the records are shown in Fig. 3. Particular attention should be paid to the record of station HWA048, which was recognized as non pulse-like one according to SB14 method despite its high PGV value, i.e., 46.02 cm/s. The corresponding *PGV* and *PC* value of HWA048 is relatively close to the classification boundary proposed in SB14 method.

3.2. Pulse-like occurrence probability computation

Several researchers have proposed prediction models for occurrence probability of velocity pulses at near-field stations (e.g., Refs. [22,26,27]). Two prediction models regressed using non-strike-slip pulse-like recordings, hereafter were referred as Model 1 (Eq. (3)) [22] and Model 2 (Eq. (4)) [26], were used for computation of pulse-like occurrence probability corresponding to the Fault 1 as illustrated in Fig. 5.

$$\text{Model 1: } P(pulse|R_{rup}, d, \varphi) = \frac{1}{1 + e^{(0.304+0.72R_{rup}-0.208\sqrt{d}+0.021\varphi)}} \quad (3)$$

Table 2
Information of the near-field stations in Hualien earthquake and the pulse-like records identification results.

Station Code	Long.(°)	Lat.(°)	R_{rup} (km)	$Vs30$[b] (m/s)	*PGV* (cm/s)	T_p (s)	*PI*	*PC*	*Maximum pulse-like Orientation(°)*	*Pulse Probability*		*pulse-like?*
										Model 1	*Model 2*	
HWA007	**121.6262**	**23.9865**	**5.02**	**379**	**95**	**4.45**	**25.0**	**0.40**	**109.0**	**0.46**	**0.35**	**Yes**
HWA008	**121.6030**	**23.9873**	**6.62**	**297**	**95**	**3.27**	**28.0**	**0.33**	**93.2**	**0.42**	**0.30**	**Yes**
HWA009	**121.6223**	**23.9903**	**5.48**	**461**	**106**	**4.78**	**26.6**	**0.43**	**87.9**	**0.44**	**0.34**	**Yes**
HWA010	**121.6027**	**23.9783**	**6.18**	**250**	**124**	**3.25**	**37.3**	**0.34**	**99.0**	**0.44**	**0.31**	**Yes**
HWA011	**121.5948**	**23.9953**	**7.58**	**361**	**89**	**3.83**	**21.2**	**0.44**	**176.9**	**0.39**	**0.28**	**Yes**
HWA012	**121.6313**	**23.9920**	**4.96**	**410**	**86**	**4.84**	**21.4**	**0.41**	**112.2**	**0.45**	**0.35**	**Yes**
HWA013	**121.5985**	**23.9755**	**6.32**	**337**	**112**	**2.74**	**30.9**	**0.38**	**112.7**	**0.45**	**0.31**	**Yes**
HWA014	**121.6057**	**23.9712**	**5.62**	**280**	**145**	**3.68**	**46.4**	**0.30**	**85.0**	**0.47**	**0.33**	**Yes**
HWA019	**121.6135**	**23.9750**	**5.29**	**504**	**138**	**3.33**	**48.8**	**0.23**	**69.7**	**0.47**	**0.34**	**Yes**
HWA023	121.6045	24.0812	11.30	**623**	9	–	−7.2	1.17	20.9	0.17	0.15	No
HWA028	**121.6095**	**24.0143**	**7.56**	**405**	**54**	**4.17**	**4.6**	**0.68**	**160.5**	**0.35**	**0.27**	**Yes**
HWA045	121.7495	24.3090	13.22	**473**	8	–	−5.6	0.96	168.4	0.26	0.17	No
HWA046	121.6292	24.1478	13.04	**644**	17	–	−7.4	1.15	7.8	0.06	0.08	No
HWA048[a]	**121.5805**	**24.0095**	**9.26**	**350**	**46**	**2.73**	**−3.7**	**0.95**	**165.0**	**0.33**	**0.24**	**Yes**
HWA050	**121.5908**	**23.9878**	**7.46**	**343**	**85**	**2.16**	**25.3**	**0.31**	**137.8**	**0.40**	**0.28**	**Yes**
HWA057	121.6230	24.1587	14.01	**815**	11	–	−11.2	1.45	0.9	0.06	0.07	No
HWA058	121.4928	23.9658	12.90	**526**	8	–	−5.4	0.94	112.3	0.33	0.17	No
HWA060	**121.6017**	**23.9035**	**2.43**	**556**	**65**	**1.23**	**12.3**	**0.50**	**32.1**	**0.62**	**0.40**	**Yes**
HWA062	**121.6198**	**23.9797**	**5.11**	**606**	**110**	**3.89**	**27.2**	**0.44**	**115.1**	**0.47**	**0.35**	**Yes**
HWA063	**121.5930**	**23.9935**	**7.60**	**289**	**95**	**2.35**	**14.4**	**0.62**	**171.6**	**0.39**	**0.28**	**Yes**
TRB042	**121.6038**	**24.0003**	**7.23**	**379**	**80**	**3.28**	**23.2**	**0.31**	**27.8**	**0.39**	**0.28**	**Yes**

[a] bold station code means the station with ambiguous preliminary identified pulse-like record and manually verified.
[b] V_{S30} at each station were obtained from Refs. [23,24].

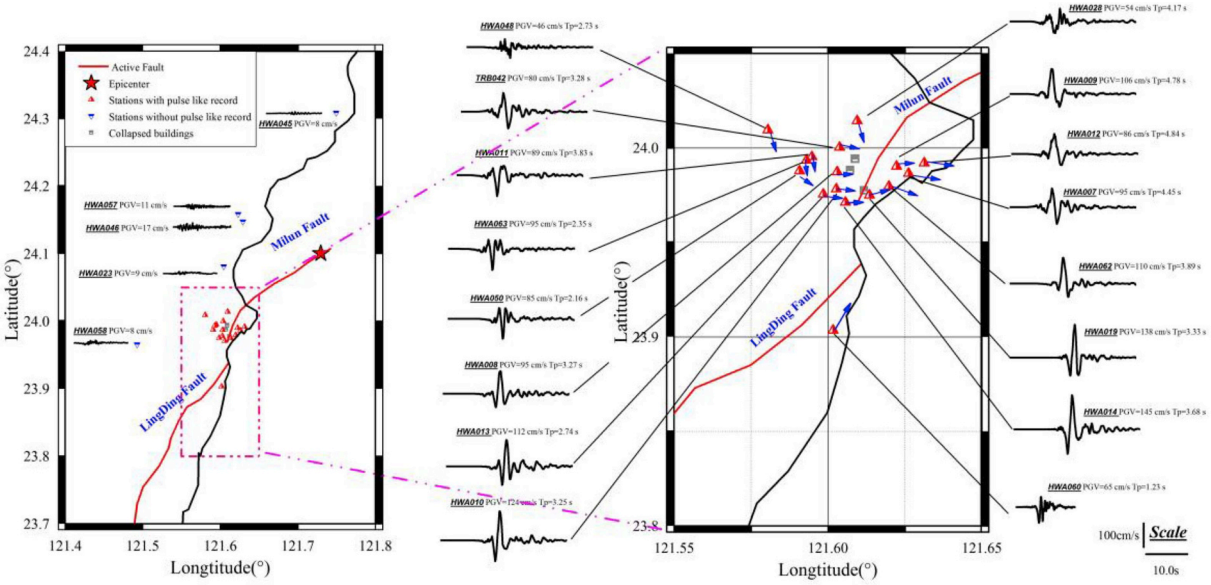

Fig. 4. The velocity time histories were rotated in the maximum pulse-like orientations area regarding the stations with/without velocity pulses in the studied near-field. The epicenter, fault and four collapsed buildings in Hualien city were illustrated in the map. The maximum pulse orientations were presented using blue arrows for the stations with identified pulse-like velocities in Table 2. (For interpretation of the references to colour in this figure legend, the reader is referred to the Web version of this article.)

$$\text{Model 2: } P(pulse|R_{rup},\ d,\ \varphi) = \frac{1}{1 + 1/e^{(0.553 - 0.055R_{rup} - 0.0267d - 0.027\varphi)}} \quad (4)$$

In which, R_{rup} is the closest distance to the fault rupture; d is the fraction of the rupture surface that lies between the hypocenter and the site; andϕ is the angle between the direction of rupture propagation and the direction aligning the hypocenter and the site. The parameters were illustrated in Fig. 5.

The contour maps of pulse-like occurrence probability according to Model 1 and Model 2 for the studied area were presented in Fig. 6 respectively. It is indicated that the pulse-like identification results are in general agreement with the trend illustrated in the contour map. For Model 1, almost all the pulse occurrence probability of sites with identified pulse-like records were higher than 0.5. It is worth noting that the maximum occurrence probability is 0.5 for Model 2, this is because the model was developed generically for non-strike-slip earthquakes that are often complex and not easy to identify rupture directivity effects. Nevertheless, it still could be observed that the probability are relatively higher for the sites with identified velocity pulses than the non-pulse-like ones. The pulse-like probability results

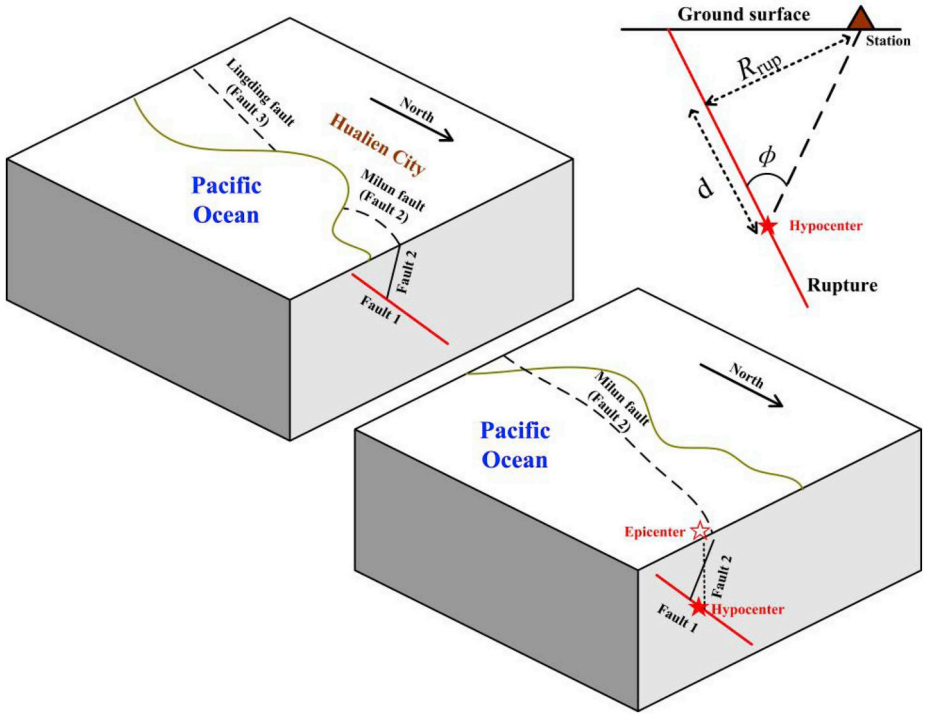

Fig. 5. The rupture schematic illustration of three faults in Hualien earthquake and the parameters used in empirical pulse-like occurrence probability prediction models.

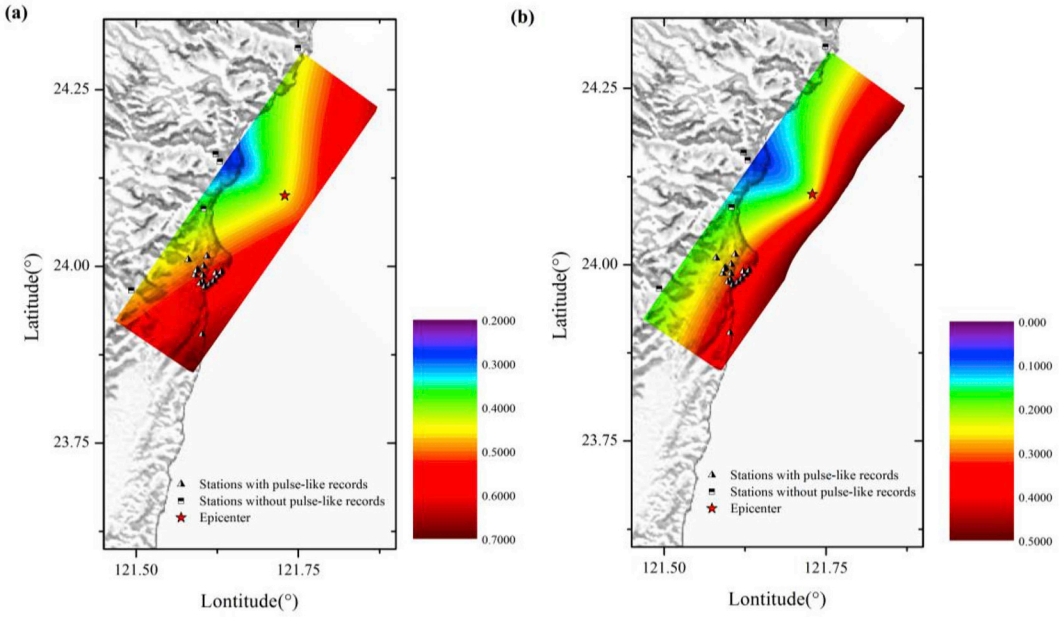

Fig. 6. Contour map of pulse-like occurrence probability using two prediction models and compared with pulse-like round motion recognition results using SB14 method: (a) Model 1 proposed in Ref. [22](b)Model 2 proposed in Ref. [26].

Table 3
The pulse-like records identification results and the Ep values calculated using the method proposed by Zhai et al(2018) [25].

Station Code	Classified as Pulse	*Ep*	*Type*	*PGV* (cm/s)	Station Code	Classified as Pulse	*Ep*	*Type*	*PGV* (cm/s)
HWA007	**Yes**	0.93	2	**95**	HWA045	No	-	-	8
HWA008	**Yes**	0.92	3	**95**	HWA046	No	-	-	17
HWA009	**Yes**	0.95	2	**106**	**HWA048***	**Yes**	0.63	2	**46**
HWA010	**Yes**	0.85	2	**124**	**HWA050**	**Yes**	0.83	3	**85**
HWA011	**Yes**	0.79	2	**89**	HWA057	No	-	-	11
HWA012	**Yes**	0.94	2	**86**	HWA058	No	-	-	8
HWA013	**Yes**	0.87	3	**112**	**HWA060**	**Yes**	0.81	3	**65**
HWA014	**Yes**	0.85	2	**145**	**HWA062**	**Yes**	0.93	2	**110**
HWA019	**Yes**	0.97	3	**138**	**HWA063**	**Yes**	0.72	2	**95**
HWA023	No	-	-	9	**TRB042**	**Yes**	0.81	2	**80**
HWA028	**Yes**	0.78	3	**54**					

for HWA048 according to prediction Model 1 and Model 2 were 0.33 and 0.24, which lays in the disputed region and need to be further verified. Following we would verify the pulse-like identification results including the HWA048 station using another method.

3.3. Verification of the identified pulse-like records

The SB14 method is usually efficient and convenient for preliminarily automatic recognition of pulse-like records from a large dataset, e.g., the PEER NGA-West2 dataset. The identification results need to be further verified because the classification boundary of the SB14 method is empirical and fixed. There is a possibility that this method might not successfully recognize all possible pulse-like records especially for those close to the boundary with high *PGV* values. An efficient algorithm for identifying pulse-like ground motions based on significant velocity half-cycles was proposed by Zhai et al [25], which could identify single, multiple, or irregular pulses. Because we had already preliminarily recognized the maximum pulse-like orientation for each record using SB14 method, the method proposed in Ref. [25] would be directly applied here to further verify the corresponding rotated record.

To effectively characterize the intrinsic pulse-like features, the concept of an energy-based significant velocity half-cycle was proposed [25]. The energy of k_{th} velocity half-cycle ΔE_k is defined as the cumulative squared velocity over the finite time interval between two consecutive zero-crossings. Velocity half-cycles whose energy ratio (defined as $E_k = \Delta E_k / E_{total}$) is greater than or equal to 0.1 are defined as "significant" half-cycles and make a substantial contribution to the total energy. Then the ground motions are classified into 6 categories according to the number of significant half-cycles in the velocity time series, i.e., Type-0 (no significant half-cycle), Type-1 (only 1 significant half-cycle), Type-2 (2 significant half-cycles), Type-3 (3 significant half-cycles), Type-4 (4 significant half-cycles), and Type-5 (at least 5 significant half-cycles in the velocity time history). The pulse energy ratio, E_p, is then used as an indicator for quantitative identification, which were defined as sum of the E_k from the significant velocity pulses. Then the E_p threshold values for each type of ground motions are determined to be 0.30, 0.42, 0.50, 0.57, and 0.73, respectively. A *PGV* threshold level of above 30 cm/s is used as a preliminary selection criterion [25], which is a bit larger than the threshold 20 cm/s in SB14 method. The E_p computation results and corresponding identification results for the 21 stations were listed in Table .3. All the pulse-like classification results are consistent with the results identified using the SB14 method except for the HWA048 station. The stations were classified as Type-2 (10 stations) and Type −3(6 stations), that is, with two or three significant half-cycles. The coherent shape of velocity pulses were caused by the close-by spatial distribution of stations as illustrated in Fig. 4.

The HWA048 record is classified as pulse-like category with *Ep* value of 0.63, slightly larger than the threshold value of 0.5 for Type-2

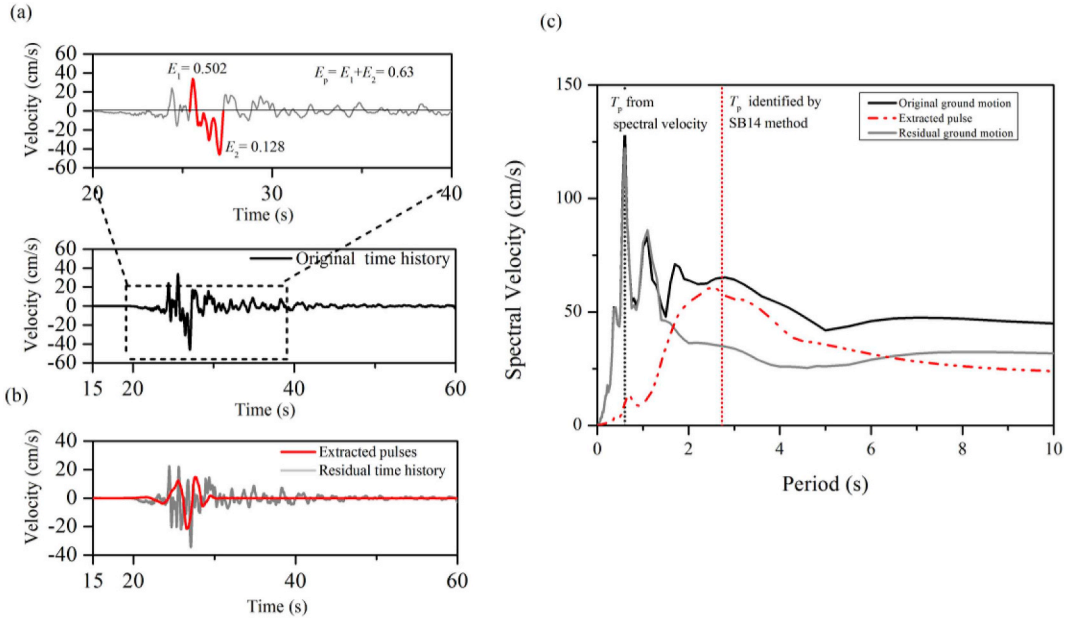

Fig. 7. (a) Significant velocity half-cycles and energy ratios computed using method in Zhai et al(2018) [25][] for the HWA048 station; (b) The extracted velocity pulse computed using SB14 method and residual time histories (c) Velocity response spectrum of the original record, extracted pulses and the residual record, with labels noting the identified T_p values using wavelet algorithm and peak of velocity spectrum.

records. Two significant velocity pulses were recognized in the velocity time histories as shown in Fig. 7(a). The extracted pulses using SB14 method and residual time history are plotted separately in Fig. 7(b). A typical velocity pulse-like waveform could be clearly observed and extracted with relatively long pulse period T_p = 2.73 s. A large velocity peak exists in the residual time history leading to a relatively large *PGV* ratio of 0.749. That is why it is classified as the non-pulse like record according to the SB14 method. Therefore the HWA048 record is considered to be classified as pulse-like one according to the recognition results of the two methods illustrated in Fig. 7(a) and (b).

3.4. Verification of pulse period T_p

The T_p identification results were compared with the peak period of the velocity response spectrum with 5% damping ratio, which was usually used as another alternative automated method for T_p determination [28]. A plot of identified T_p values from two approaches is shown in Fig. 8 for the 16 pulse-like ground motions.

The T_p values obtained using the two approaches are overall similar, with the SB14 method computation results being slightly longer than the spectral velocity based T_p in general. Similar tendency was also observed in studies based on the NGA ground motion library [1,21]. In cases where the periods obtained from the wavelet and the velocity spectrum methods differ significantly, the period with maximum spectral velocity is associated with the high-frequency oscillatory portion of the ground motion that is usually not the velocity pulses we concern. The wavelet algorithm-based pulse period is more closely associated with the visible velocity pulse. Because this method uses the ratios of *PGV* and energy between the original and residual records as predictor variables for this classification, the high-frequency oscillatory portion with high amplitude is hard to contaminate the identification results due to its relatively short duration and small energy contribution.

For station HWA048, the T_p obtained from the SB14 method and the velocity response spectrum differ significantly. The spectral velocity of HWA048 record is predominant at both short periods (< 1.0 s) and moderated-to-long periods (1.0–5.0 s) leading to inaccurate estimation of T_p based on velocity response spectrum. In this case, the period with maximum spectral velocity is ascribed to the peak at the short period,

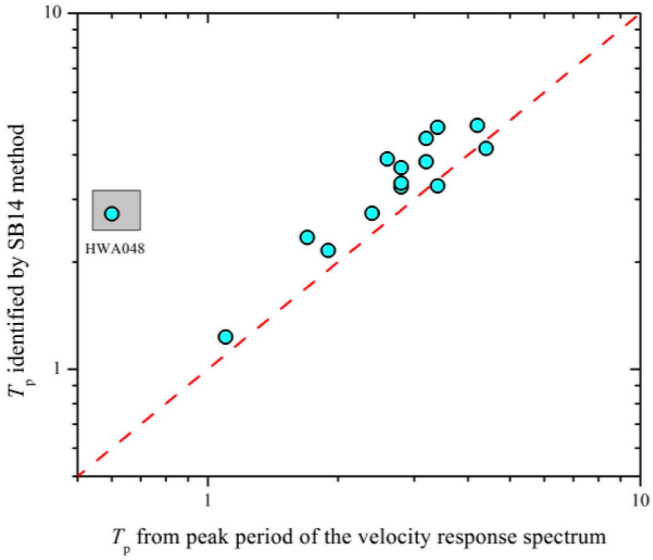

Fig. 8. Comparison of the T_p values identified from the peak period of the velocity response spectrum and the results using the SB14 method.

whereas the longer T_p identified using wavelet method is associated with the pulse duration as illustrated in Fig. 7(c), indicating a more plausible result.

3.5. Comparison with the NGA-West2 empirical models for T_p

The relationship between pulse period and earthquake magnitude had been frequently investigated based on different database (e.g. Refs. [1,10,22,28]). The period of the velocity pulse is related to source parameters including the rise time and fault dimensions, both of which increase with magnitude. Therefore the ln(T_p) is usually represented as a linear function of M_w. Although the regression model is similar, the parameters will be influenced by the selection of the pulse-like records and the procedure employed to determine the pulse period T_p.

To further confirm the pulse-like identification results and to

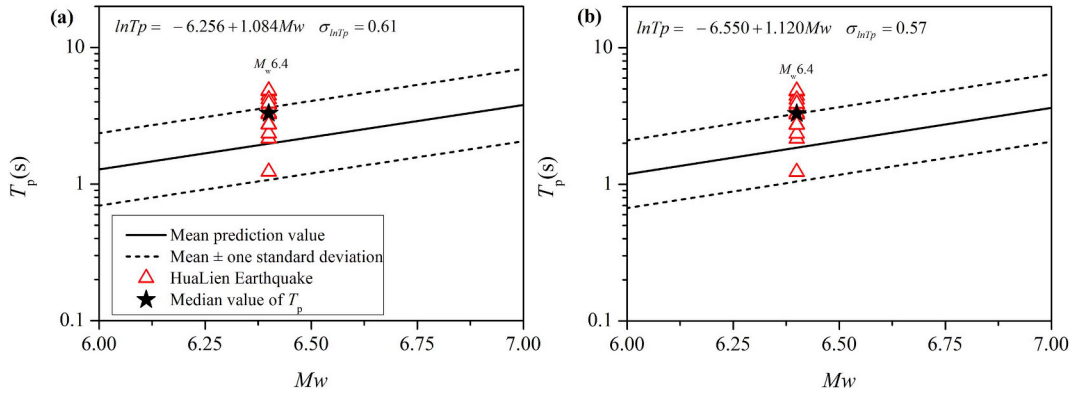

Fig. 9. Comparison of the identified T_p values with two prediction model fitted by: (a) pulse-like records caused by directivity effect and (b) all the pulse-like records from the NGA-West2 dataset regardless of the cause or mechanism.

determine whether they might be of special interest for structural engineering, the extracted T_p values and the empirical prediction models based on the NGA-West2 records were compared as shown in Fig. 9 [22]. The pulse-like records identification and T_p computation procedure are identical with what we applied in this paper. Because the identified pulse-like record in this study did not show a certain directivity effect attribute, models suitable for directivity pulses and for all pulses were both chosen for comparison.

The results indicate that the extracted T_p values from the Hualien earthquake are approximately one standard deviation higher than the predicted mean values conditioned at M_w6.4. For Hualien earthquake, a complex seismic moment release history could be found from the moment rate function and three time periods of associated energy releases are illustrated in Ref. [2]. The total seismic moments considering is equivalent to an M_w6.58 earthquake, which is larger than the M_w6.4 given by USGS(U.S. Geological Survey center) and GCMT(Global Centroid Moment Tensor project). The $\ln(T_p)$ is approximately overall within the prediction value plus one standard deviation conditioned at M_w6.58.

4. Structural response to near-field pulse-like ground motions

4.1. SDOF inelastic displacement demands

To analyze the impact of pulse-like record on the buildings with different fundamental periods, the SDOF systems with constant strength were utilized to compute the corresponding inelastic displacement ($S_{d,i}$). The bilinear hysteretic model used was defined by three-parameters: 3% hardening ratio, 5% damping ratio, and yield strength reduction factor (R). Different R values indicate different SDOF ductility as defined in Eq. (5).

$$R = \frac{f_0}{f_y} \tag{5}$$

where f_0 is the strength required for the structure to remain within its linearly elastic limit during the ground motion. f_y is its yielding strength. The closer the R approaches 1.0, the closer the SDOF system is to represent an entirely elastic system.

Inelastic displacement ratio is a particularly appealing approach to evaluate the maximum inelastic displacement of structures with different fundamental periods. We computed the inelastic and elastic displacement ($S_{d,i}$ and $S_{d,e}$) using the 21 near-field records as inputs. Fig. 10 shows the ratio between inelastic and elastic displacement ($S_{d,i}/S_{d,e}$) versus the ratio of the oscillator period to pulse period (T/T_p) in three cases of R = 2,4 and 6, respectively. When T/T_p is less than 0.6, different inelastic demand is observed between the response of non pulse-like records and pulse-like records. The difference is much more significant with larger R. The mean $\ln(S_{d,i}/S_{d,e})$ ratios for the five non-pulse-like records are less than 1.0, while the mean ratios for the pulse-like records is larger than 2.0 when R equals to 4 and 6. The results indicate that a possible larger inelastic displacement response is expected for structures with $T/T_p < 0.6$ when subject to the pulse-like records in Hualien earthquake.

One comprehensive prediction model for inelastic displacement ratio regarding near-fault pulse-like recordings was investigated in Ref. [8]. It was determined in a two-step nonlinear regression of a relatively large set of fault-normal pulse-like records in NGA dataset identified by Baker07 method [21]. The standard deviation was also given as a function of the T/T_p ratio. The $\ln(S_{d,i}/S_{d,e})$ and the corresponding dispersion computed in this paper were compared with the predicted results as shown in Figs. 10 and 11. It is indicated that the $\ln(S_{d,i}/S_{d,e})$ for pulse-like records in Hualien earthquake was nearly one standard deviation higher than the predicted mean values in the $0.1 < T/T_P < 0.5$ range. For R = 4 and 6 cases, low dispersion for $\ln(S_{d,i}/S_{d,e})$ could be observed in the $0.5 < T/T_P < 1.5$ range which is probably because of the similar pulses recorded in the close-by stations.

4.2. Four partially collapsed buildings in Hualien City

Four mid-rise RC buildings in Hualien City were seriously damaged during the earthquake. Details of these buildings and the damage situation are summarized in Table 4. These four buildings were partially collapsed or tilted due to the bottom story crush. Their locations and the nearby strong motion stations are illustrated in Fig. 12. The tilted Yun Men Tsui Ti building (No.04) resulted in 14 fatalities.

Because there is not enough available information for structural configurations, we use the empirical prediction equation in the Taiwan design code [29](2011) to roughly estimate the fundamental period T of these four buildings. The equation, $T = 0.050H^{3/4}$, is applied for the RC-frame structures with non-structural partition infill walls. H is the height of the structure. The maximum fundamental period of structures should not exceed the 1.4 T [29]. The H of four collapsed building were obtained from the building database in Ref. [30], personal communication with T. C. Chiou (2019) and the snapshots of Google map Street View. The range of H and fundamental period T were listed in Table 4. The T/T_p values for these four buildings regarding 16 near-field pulse-like records are illustrated in the Fig. 13. According to the SDOF computation results in the Fig. 10, a large inelastic demand is expected when the T/T_p value is below 0.6. Almost all the T/T_p values ranged from 0.15 to 0.40 with small dispersion except the results of the HWA060 record which is located far from Milun fault and Hualien city, implying a large elastic demand is expected for these four mid-rise buildings when subject to the pulse-like ground motions in Hualien earthquake.

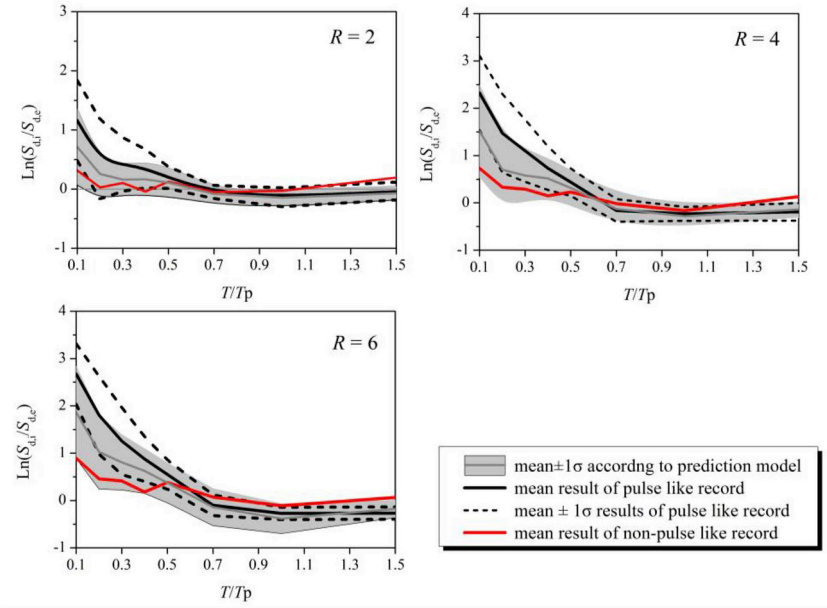

Fig. 10. Comparison of ratio of the inelastic and elastic SDOF displacement demand derived from the pulse-like recordings and the prediction model results in Ref. [17] regarding different R.

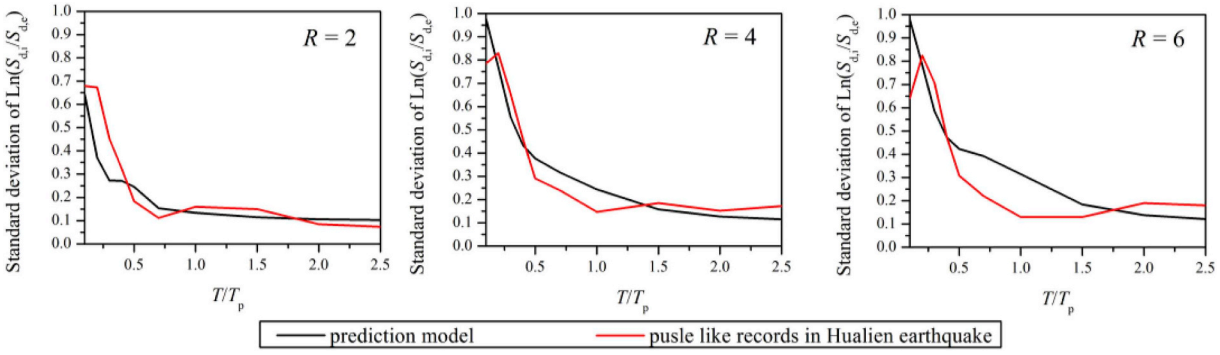

Fig. 11. Comparison of standard deviation of $\ln(S_{d,i}/S_{d,e})$ ratios derived from the pulse-like records in Hualien earthquake and prediction model.

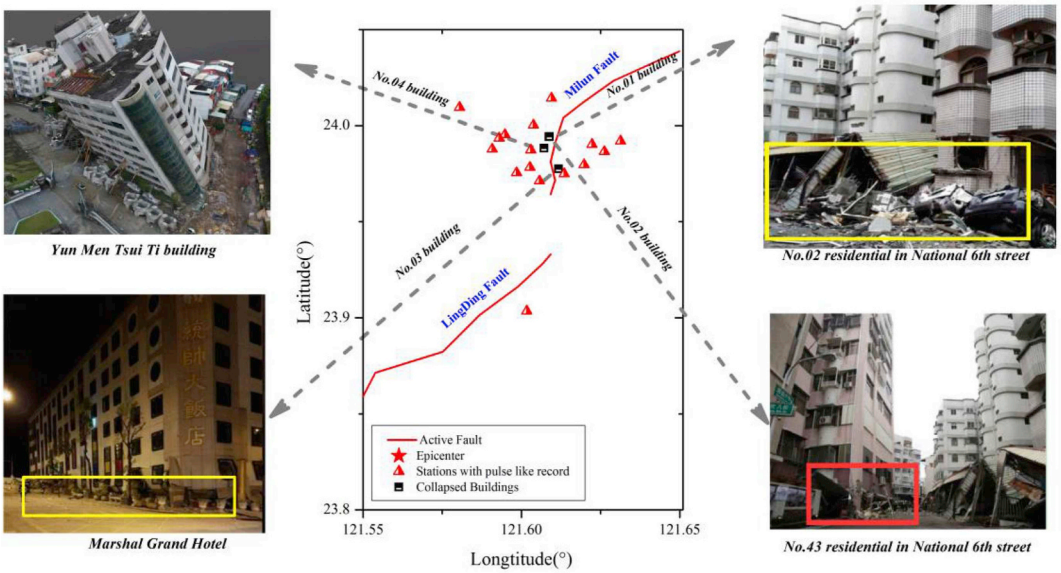

Fig. 12. Four partially collapsed buildings in Hualien city and near-by stations with pulse-like ground motions identified in this paper. The bottom stories crush of the buildings were marked using rectangles in photos.

Table 4
The information of four severely damaged buildings.

Building No.	Building Name	Story	Building Age	Damage situation	Height	Fundamental period range
01	No.02 residential in National 6th Street	7	1997	Ground floor crushed	16.2–18.8 m	0.45–0.62 s
02	No.43 residential in national 6th Street	10 (7-story building with 3 additional stories)	1999	Ground floor crushed	43.6 m	0.85–1.18 s
03	Marshal Grand Hotel	11	1977	Bottom two stories crushed	32.0 m	0.67–0.94 s
04	Yun Men Tsui Ti building	12	1991	Bottom three stories crushed	33.0–35.0 m	0.70–1.03 s

4.3. Story ductility demand

The bottom stories of No.1 and No.2 buildings were retrofitted into garages by removing almost all RC infill walls. Unbalance columns could also be observed in the bottom story of No.3 and No.4 buildings. Part of the walls and columns in the bottom stories were removed for pedestrians passing or parking utility. To cover the fundamental period range and story levels as illustrated in Table .4, 7-story, 9-story, and 11-story shearing MDOF systems are utilized respectively to quantify the ductility demand over different stories. The height and mass over different stories are set as equal for the studied MDOF systems. The mass was set as 600×10^3 kg for each story. The story shear stiffness and strength decreased from the bottom story to the top, which is determined from an inverted-triangle lateral story shear force load pattern that corresponds to the Taiwan Design Code [29]. The ratio λ between the base shear strength V_y and the weight of the whole structure W was set as 0.2 and 0.4, which represent a comparatively weak and strong structure, respectively. Three 7-story MDOF systems were studied in this paper with different stories' stiffness, which were set to make the fundamental periods close to 0.4s, 0.5s, and 0.6s respectively. 9-story MDOF systems with fundamental period close to 0.55s, 0.65s, and 0.75s will be discussed in the following study. 11-story MDOF systems with fundamental period close to 0.7s, 0.8s, 0.9s, and 1.0s will be discussed.

The failure of the bottom story during an earthquake may trigger a bottom soft-story mechanism leading to the collapse of the whole structural system as illustrated in the Figs. 1214. For these four buildings, the infill walls of bottom story were partially removed that makes significant stiffness and strength difference existed between the bottom and upper stories. To roughly estimate the infill walls' contributions to stiffness and strength, we built MDOF systems in which the stiffness and strength of bottom story are reduced by 30%, which is the threshold of stiffness reduction in the Taiwan design code [29]. The Clough stiffness degradation hysteresis model with a 10% strain-hardening ratio was chosen here [31]. Hysteresis models considering strength degradation are necessary for more accurate simulation of structural collapse if more detailed finite element analysis would be carried out according to the detailed structural configurations in the future study. Conventional Rayleigh damping was used with a 5% damping ratio at the fundamental period T and 0.1 T. Note that only one damping ratio is used here because the maximum structural response subjected to pulse-type excitations was relatively insensitive to the damping ratio [32]. The story ductility demand is quantified by the story ductility ratio, defined as the maximum inter-story drift normalized by the story yield drift. Figs. 15 and 16 illustrate the average ductility demand over different stories of the MDOF structures in two cases of $\lambda = 0.2$ and 0.4 regarding different fundamental period.

The results show that the story ductility demand subject to the non-pulse-like records are almost less than 1.0, much lower than that for the pulse-like records, which is in agreement with the inelastic demand results using SDOF regarding $T/T_p < 0.6$. For pulse-like recordings, the maximum story ductility demand tends to occur in the bottom portion of the 7-story, 9-story and the 11-story shearing MDOF structures, which could reach nearly 6.0 and 1.5 for $\lambda = 0.2$ and 0.4 respectively. The overall trend is consistent with the observations for the MDOF with relatively short-period ($T < T_p$) in Ref. [14]. The story ductility values for each MDOF did not change significantly within the fundamental period range given in Table .4.

When the bottom story of MDOF is set as the weak story, there is still no obvious ductility demand observed for the non-pulse-like ones except for the bottom portion that could reach approximated 2.0 conditioned at $\lambda = 0.2$. For the MDOFs with weak bottom story, the bottom story ductility demand is much more significant, which is almost two times larger than the cases without weak bottom story. The mean bottom story ductility demand is around 11.0 and 3.5 for the cases of $\lambda = 0.2$ and $\lambda = 0.4$ respectively. The ductility ratio of more than 10.0 in the case of $\lambda = 0.2$ considerably exceeds the design capacity and may

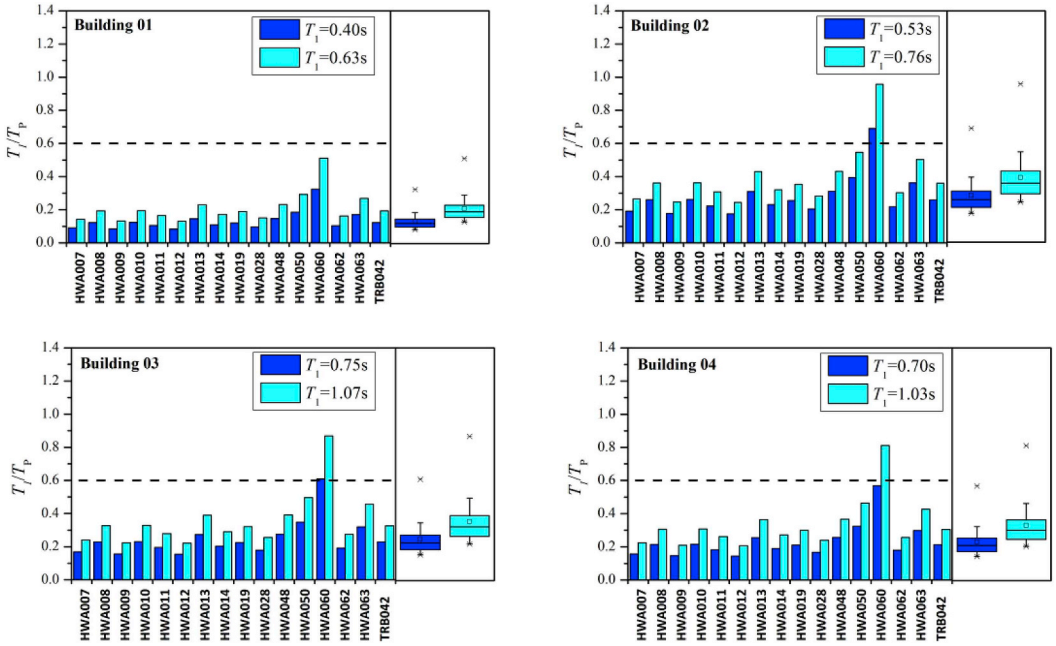

Fig. 13. T/T_p range for the four collapsed buildings with maximum and minimum estimated fundamental period T. The box diagram was used to illustrate the median and dispersion of T/T_p values; T_p values were calculated using recordings rotated in the maximum pulse-like orientation using the SB14 method.

Fig. 14. The bottom-stories layout of four collapsed buildings (from Google Map).

trigger the failure of the first story. To summarize, the near field pulse-like ground motions and the soft bottom story mechanism are the main reasons for the four collapsed buildings in Hualien earthquake.

4.4. Comparison with the code design spectrum

The construction time of all the four buildings was before 1999, when a more comprehensive building design code came into effect. It is worth noting that the near-fault amplification effect has been considered specifically in the seismic design code after 2005 version. For Hualien city that located near Milun Fault, the design spectral acceleration coefficient for short and long period were amplified regarding different site-to-fault distance. The maximum considered earthquake in design spectrum with a return period of 2500 years (50-year 2 % exceedance rate) was compared with the acceleration spectrum (5 % damping ratio) of each near field ground motion as shown in Fig. 17. Besides the spectral accelerations of east–west (EW), north–south (NS) components, we also computed the results in components rotated to the maximum pulse-like orientation which were considered in the SDOF and MDOF calculation. Although the new design spectrum of Hualien City has a conservative consideration of the near fault amplification effect, some of the spectral accelerations at periods ranging from 1.5 s to 3.5 s still exceed the design spectra values.

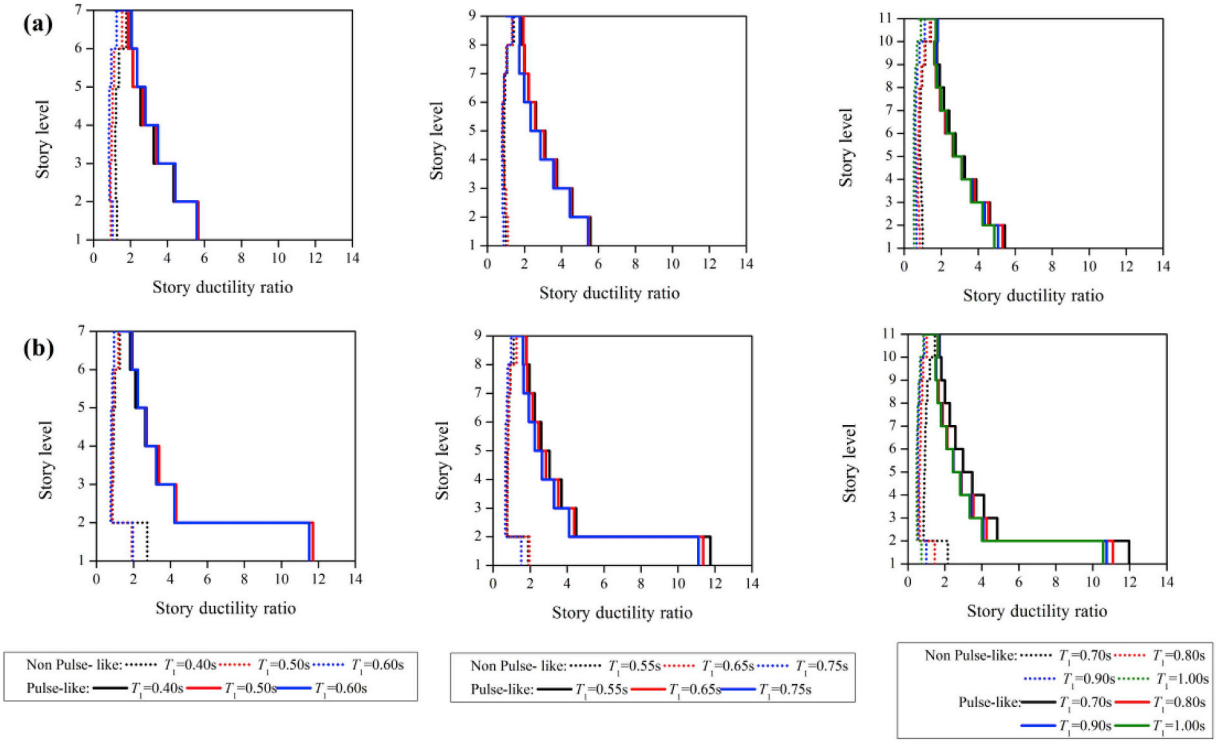

Fig. 15. The story ductility ratio curves for 7-story, 9-story and 11-story MDOFs with different fundamental periods in the case of λ = 0.2: (a) without consideration of the bottom stiffness reduction; (b) with 30% reduced bottom shear story stiffness and shear strength.

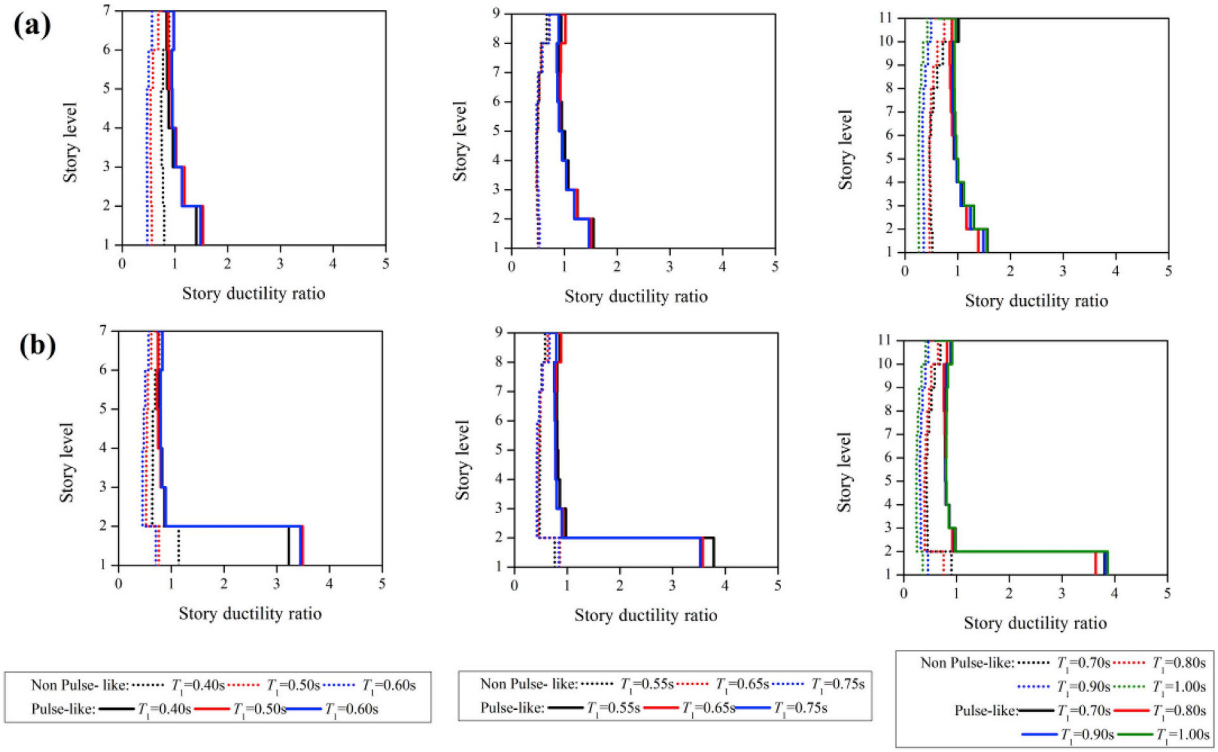

Fig. 16. The story ductility ratio curves for 7-story, 9-story and 11-story MDOFs with different fundamental periods in the case of λ = 0.4: (a) without consideration of the bottom stiffness reduction; (b) with 30% reduced bottom shear story stiffness and shear strength.

5. Conclusions

This paper intended to investigate the pulse-like characteristics of ground motions in the 2018 M_w6.4 Hualien earthquake and study their impact on structures' damage. The SB14 wavelet method was utilized to identify near-source pulse-like records in the first step. The maximum pulse-like orientation and the T_p values were computed based on the pulses extracted from the orthogonal components using the wavelet transform algorithm. The pulse-like occurrence probability of near-fault area of Hualien earthquake were also computed using two prediction

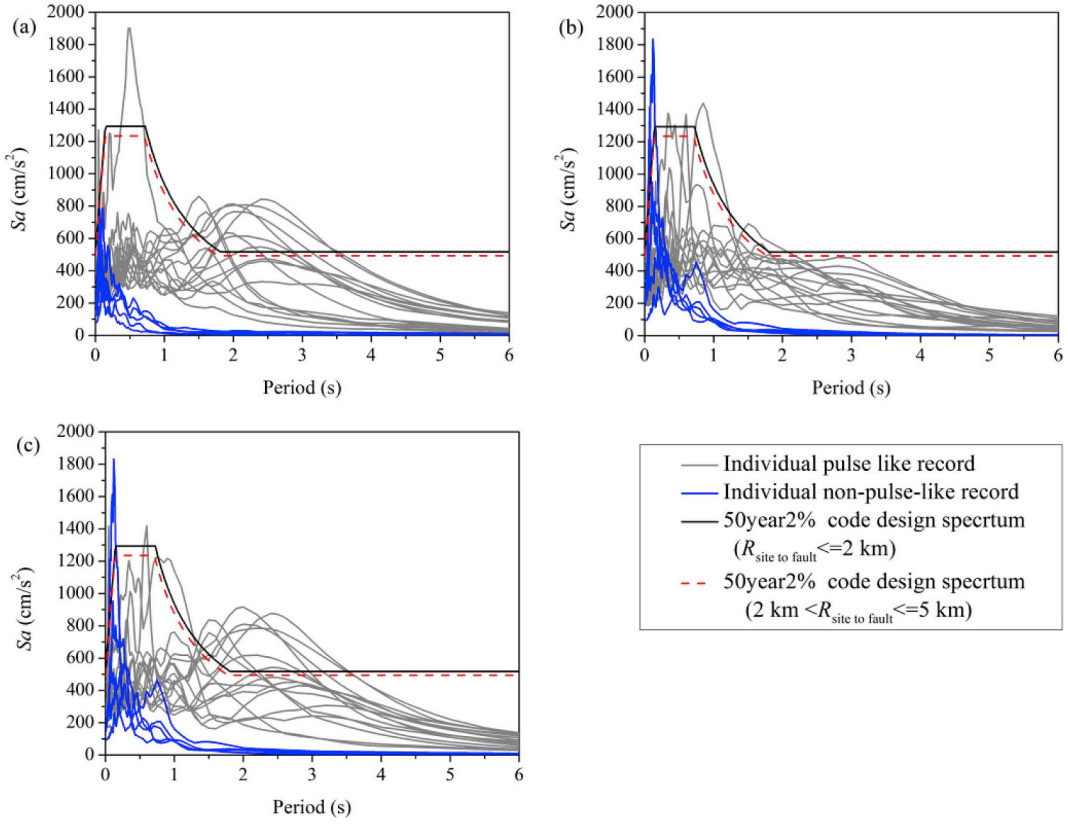

Fig. 17. Comparison between the acceleration spectrum (damping ratio = 5%) of near-field records observed in Hualien earthquake and the code design spectrum; (a),(b) and (c) represents the EW, NS components and the component rotated to the maximum pulse-like orientation respectively.

models, the results were in good agreement with the identification results by SB14 method. Then the identification results were verified using method [25] based on the energy content of the significant velocity pulses. Overall, 16 near-field stations including the controversial HWA048 station in Hualien City were classified as having two or three significant velocity pulses. The extracted T_p values were generally longer than predictions based on empirical regression model based on the NGA-West2 dataset.

The SDOF and MDOF systems were implemented to compute the inelastic displacements and story ductility demand. For the identified pulse-like records, the results show that the inelastic demand of SDOF with oscillator period less than 0.6 T_p was much more significant than that for non-pulse-like records when the nonlinearity level increased. The mean inelastic displacement ratio curve is one standard deviation larger than the predicted mean value in the $0.1 < T/T_P < 0.5$ range. For $R = 4$ and 6 cases, low dispersion for $\ln(S_{d,i}/S_{d,e})$ could be observed in the $0.5 < T/T_P < 1.5$ range which is probably because of the similar pulses recorded in the close-by stations.

The MDOF computation results show that larger story ductility demand was expected for the pulse-like ground motions compared with the non pulse-like ones in Hualien earthquake. For pulse-like recordings, the maximum story ductility demand tends to occur in the bottom portion of the 7-story, 9-story and the 11-story shearing MDOF structures, which could reach nearly 6.0 and 1.5 for $\lambda = 0.2$ and 0.4 respectively. While the ductility demands for different stories are overall the same for the non pulse-like recordings, which is approximately in the range of 0.5–1.0. Furthermore, the infill walls of bottom stories were partially removed in these four buildings, which largely reduce the bottom shear stiffness and strength compared with upper stories. The corresponding bottom story ductility ratios subject to pulse-like records could reach more than 10.0 conditioned at $\lambda = 0.2$ when the bottom stiffness and strength reduced by 30%. There is still no obvious ductility demand observed for the non-pulse-like ones including the bottom portion.

Coupled with the large ductility demand under near-field pulse-like ground motions and the soft-story mechanism in bottom portion, the old seismic design code without consideration of near-fault amplification effect also contributes to the excessive vulnerability of those four buildings in Hualien earthquake. More detailed structural finite element analysis is still needed to be utilized in the future work to provide more comprehensive explanations for the collapse mechanism of these four buildings.

Data and resources

The strong-motion waveform records used in this study were obtained from the stations of Central Weather Bureau in Taiwan, whose raw data are available at ftp://gdms.cwb.gov.tw/ last accessed Oct 2018. The procedure to identify pulses has been implemented by J.W. Baker in Matlab scripts and is publicly available at http://github.com/shreyshahi/PulseClassification last accessed July 2018.

Acknowledgement

This work was supported by the National Key R&D Program of China [grant number. 2017YFC1500801]; Chinese National Natural Science Fund [grant number. 51778589]; Natural Science Foundation of Heilongjiang Province [grant number. E2017065]; Science Foundation of the Institute of Engineering Mechanics, CEA [grant number. 2016A04]; China Shandong Co-Innovation Center for Disaster Prevention and Mitigation of Civil Structures[grant number. XTZ201901].

The editors and eight anonymous reviewers, who provided constructive suggestions and comments which significantly improved

quality and readability of the paper, are sincerely acknowledged. The authors also want to thank the Central Weather Bureau (CWB) of Taiwan for providing the catalog and the strong-motion recordings. The authors want to thank Professor Jack W. Baker for providing code regarding pulse-like ground motions identification procedure online. We want to thank Dr. T. C. Chiou who provided the height information of the collapsed buildings we concerned. Finally, the open source Generic Mapping Tools (GMT) were utilized for part of the figures' plot in this paper and be acknowledged.

References

[1] Bray JD, Rodriguez MA. Characterization of forward-directivity ground motions in the near-fault region. Soil Dyn Earthq Eng 2004;24(11):815–28.
[2] Lee SJ, Lin TC, Liu TY, Wong TP. Fault-to-fault jumping rupture of the 2018 M w 6.4 Hualien earthquake in eastern Taiwan. Seismol Res Lett 2019;90(1):30–9.
[3] Heaton TH, Hall JF, Wald DJ, Halling MW. Response of high-rise and base-isolated buildings to hypothetical Mw 7.0 blind thrust earthquake. Science 1995;267(5195):206–11.
[4] Lin Y, Yeh T, Ma K, Song TA, Lee S, Huang B, et al. Source characteristics of the 2016 Meinong (Ml 6.6), Taiwan, earthquake, revealed from dense seismic arrays: double sources and pulse-like velocity ground motion. Bull Seismol Soc Am 2018;108(1):188–99.
[5] Kuo CH, Huang JY, Lin CM, Hsu TY, Chao SH, Wen KL. Strong ground motion and pulse-like velocity observations in the near-fault region of the 2018 M w 6.4 Hualien, Taiwan, earthquake. Seismol Res Lett 2019;90(1):40–50.
[6] Zhai C, Li S, Xie L, Sun Y. Study on inelastic displacement ratio spectra for near-fault pulse-type ground motions. Earthq Eng Eng Vib 2007;6(4):351–5.
[7] Ruiz-García J. Inelastic displacement ratios for seismic assessment of structures subjected to forward-directivity near-fault ground motions. J Earthq Eng 2011;15(3):449–68.
[8] Iervolino I, Chioccarelli E, Baltzopoulos G. Inelastic displacement ratio of near-source pulse-like ground motions. Earthq Eng Struct Dyn 2012;41(15):2351–7.
[9] Baker JW, Cornell CA. Vector-valued intensity measures for pulse-like near-fault ground motions. Eng Struct 2008;30(4):1048–57.
[10] Chioccarelli E, Iervolino I. Near-source seismic demand and pulse-like records: a discussion for l'aquila earthquake. Earthq Eng Struct Dyn 2010;39(9):1039–62.
[11] Dimakopoulou V, Fragiadakis M, Spyrakos C. Influence of modeling parameters on the response of degrading systems to near-field ground motions. Eng Struct 2013;53:10–24.
[12] Wen WP, Zhai CH, Li S, Chang Z, Xie LL. Constant damage inelastic displacement ratios for the near-fault pulse-like ground motions. Eng Struct 2014;59:599–607.
[13] Zhai CH, Wen WP, Zhu TT, Li S, Xie LL. Inelastic displacement ratios for design of structures with constant damage performance. Eng Struct 2013;52:53–63.
[14] Alavi B, Krawinkler H. Behavior of moment-resisting frame structures subjected to near-fault ground motions. Earthq Eng Struct Dyn 2004;33(6):687–706.
[15] Mavroeidis GP, Papageorgiou AS. Near-source strong ground motion: characterizations and design issues. U.S. National conference on earthquake engineering, Boston, Massachusetts, 21–25 July 2002. 2002. p. 12.
[16] Champion C, Liel A. The effect of near-fault directivity on building seismic collapse risk. Earthq Eng Struct Dyn 2012;41(10):1391–409.
[17] Kalkan E, Kunnath SK. Effects of fling step and forward directivity on seismic response of buildings. Earthq Spectra 2012;22(2):367–90.
[18] Wu YM, Wu CF. Approximate recovery of coseismic deformation from Taiwan strong-motion records. J Seismol 2007;11(2):159–70.
[19] Akkar S, Bommer JJ. Influence of long-period filter cut-off on elastic spectral displacements. Earthq Eng Struct Dyn 2006;35(9):1145–65.
[20] Tian S, Gardoni P, Yuan W. Coseismic deformation of the 6 February 2018 M w 6.2 Hualien earthquake based on strong-motion recordings. Seismol Res Lett 2019;90(1):108–17.
[21] Baker JW. Quantitative classification of near-fault ground motions using wavelet analysis. Bull Seismol Soc Am 2007;97(5):1486–501.
[22] Shahi SK, Baker JW. An efficient algorithm to identify strong-velocity pulses in multicomponent ground motions. Bull Seismol Soc Am 2014;104(5):2456–66.
[23] Kuo CH, Wen KL, Hsieh HH, Lin CM, Chang TM, Kuo KW. Site Classification and Vs30 estimation of free-field TSMIP stations using the logging data of EGDT. Eng Geol 2012;129–130:68–75.
[24] Kuo CH, Lin CM, Chang SC, Wen KL, Hsieh HH. Site database for Taiwan strong motion stations. NCREE-17-004; 2017. p. 80. [In Chinese)].
[25] Zhai C, Li C, Kunnath S, Wen W. An efficient algorithm for identifying pulse-like ground motions based on significant velocity half-cycles. Earthq Eng Struct Dyn 2018;47(3):757–71.
[26] Iervolino I, Cornell CA. Probability of occurrence of velocity pulses in near-source ground motions. Bull Seismol Soc Am 2008;98(5):2262–77.
[27] Shahi SK, Baker JW. An empirically calibrated framework for including the effects of near-fault directivity in probabilistic seismic hazard analysis. Bull Seismol Soc Am 2011;101(2):742–55.
[28] Somerville PG, Smith NF, Graves RW, Abrahamson NA. Modification of empirical strong ground motion attenuation relations to include the amplitude and duration effects of rupture directivity. Seismol Res Lett 1997;68(1):199–222.
[29] Architectural Technology Committee of Taiwan. Standard and explanation of earthquake resistant design for buildings. 2011. [in Chinese)].
[30] Chiou TC, Ho YS, Weng PW, Shen WC. Building data of the 20180206 Hualien earthquake in Taiwan. 2018https://www.ncree.org/recce/20180206/.
[31] Clough RW. Effect of stiffness degradation on earthquake ductility requirements. Japan Earthquake Engineering Symposium; 1966.
[32] Chopra AK. Dynamics of structures: theory and applications to. earthquake engineering. Upper Saddle River, New Jersey: Prentice Hall; 1995.